CHAPTER 6

Tetranuclear copper(II) complexes with close and double-open cubane core: magnetic properties, DNA/protein binding and molecular docking

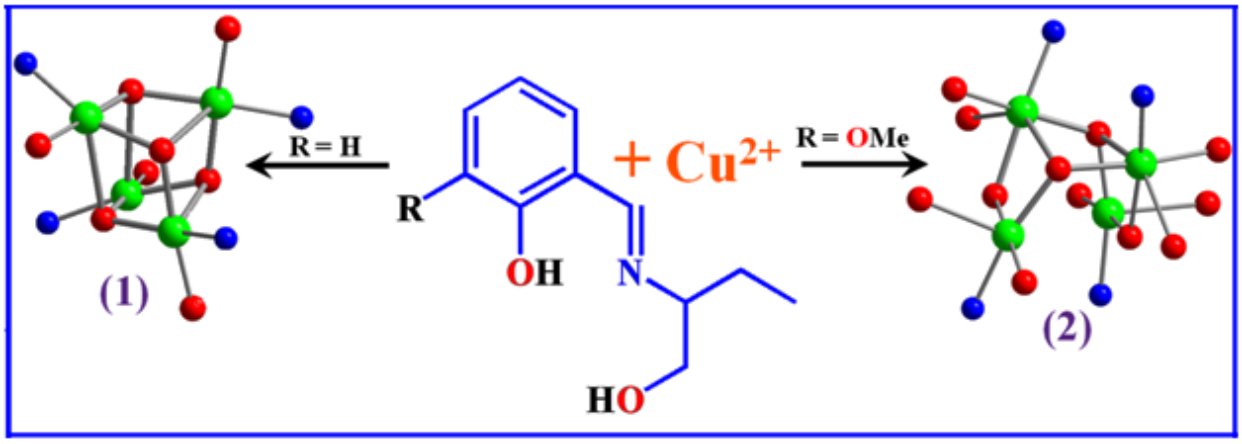

A. Paul et al./ Journal of Solid State Chemistry 271 (2019) 378-385.

6.1 Introduction

Polynuclear copper(II) complexes are stimulating not only for their interesting structure but also for potential applications in the area of molecular magnetism [6.1], bioinorganic chemistry [6.2] and catalysis [6.3]. Among these polynuclear copper complexes, tetranuclear cubane-type core (Cu_4O_4) compounds are especially important as magnetic material [6.4] and as serving as a model system for metallo-enzymes [6.5]. On the basis of structural features tetranuclear Cu_4O_4 cubane geometries may be of different types. Depending on the lengths of the Cu-O bond distances within the cubane core, Mergehem and Haase [6.6] classified these species into type-I and type-II. Cubane complexes having four long Cu-O distances between two dinuclear subunits are classified as type-I, whereas cubane complexes having long Cu-O distances within each dinuclear subunit are classified as type-II. On the other hand based on the Cu…Cu distances within the cubane core, Alvarez et al [6.7] classified the cubanes into three categories: (i) [2+4] with two short and four long Cu…Cu distances, (ii) [4+2] four short and two long Cu…Cu distances and (iii) [6+0] containing six similar Cu…Cu distances. Magneto-structural correlation of copper cubane compounds are widely reported in the literature and magnetic properties were shown to depend on structural geometrical parameters. Since magnetic behavior of these copper complexes is closely related to the structure, slight changes in structure cause significant modifications of magnetic properties.

Schiff bases are potential ligand for the formation of tetranuclear cubane compounds. In the present contribution we have used alkoxo, hydroxo, phenoxo and imine donor Schiff bases [(E)-2-((1-hydroxybutan-2-ylimino)methyl)phenol] (H_2L^1) and [(E)-2-((1-hydroxybutan-2-ylimino)methyl)-6-methoxyphenol] (H_2L^2) and synthesized two copper(II) compounds $[Cu_4(L^1)_4]\cdot 0.5(H_2O)$ (**1**) and $[Cu_4(L^2)_2(HL^2)_2(H_2O)_2](sq)\cdot 2(H_2O)$ (**2**). Complex **1** and **2** are

tetranuclear with close cubane core and double-open cubane core, respectively. Results of variable temperature magnetic measurements have been correlated with corresponding structural features.

6.2 Experimental

6.2.1 Materials and measurements

High purity 2-Amino-1-butanol was obtained from Aldrich Chemical Co. Inc. All other chemicals used were analytical grade. Solvents used for spectroscopic studies were purified and dried by standard procedures before use [6.8]. Elemental analyses (carbon, hydrogen and nitrogen) were performed using a Perkin-Elmer 240C elemental analyzer. IR spectra were recorded as KBr pellets on a Bruker Vector 22FT IR spectrophotometer operating from 400 to 4000 cm^{-1}. Electronic absorption spectra were obtained with Shimadzu UV-1601 UV-vis spectrophotometer at room temperature. Quartz cuvettes of 1 cm path length and 3 cm^3 volume were used for all measurements. Emission spectra were recorded on a Hitachi F-7000 spectrofluorimeter. Room temperature (300 K) spectra were obtained using a quartz cell of 1 cm path length. The slit width was 2.5 nm for both excitation and emission. The fluorescence quantum yield was determined using phenol as a reference and methanol medium for both complexes and reference. Emission spectra were recorded by exciting the complex and the reference phenol at the same wavelength, maintaining nearly equal absorbance (~ 0.1). The area of the emission spectrum was integrated using the software available in the instrument and the quantum yield calculated [6.9] according to the following equation:

$$\Phi_s = \Phi_r \frac{A_s}{A_r} \frac{I_r}{I_s} \frac{\eta_s^2}{\eta_r^2}$$

Where Φ_s and Φ_r are the fluorescence quantum yield of the sample and reference, respectively. A_s and A_r are the respective optical densities at the wavelength of excitation, I_s and I_r correspond to the areas under the fluorescence curve; and η_s and η_r are the refractive index values for the sample and reference, respectively. The fluorescence enhancement efficiency (%) was calculated by using equation $[(F - F_o)/F_o] \cdot 100$ and the corresponding quenching efficiency (%) by $[(F_o - F)/F_o] \times 100$, where F_0 and F are the maximum fluorescence intensity of the complex before exposure and in presence of the analyte, respectively. Temperature-dependent molar susceptibility measurements of polycrystalline samples were carried out at the Servei de Magnetoquímica of the Centres Científicsi Tecnològics at the Universitat de Barcelona in a Quantum Design SQUID MPMSXL susceptometer with an applied field of 3000 and 198 G in the temperature ranges 2-300 and 2-30 K, respectively.

6.2.2 Synthesis of the ligands

The ligands [(E)-2-((1-hydroxybutan-2-ylimino)methyl)phenol] (H_2L^1) and [(E)-2-((1-hydroxybutan-2-ylimino)methyl)-6-methoxyphenol] (H_2L^2) were prepared by the same general procedure as chapter-2.

6.2.3 Synthesis of the complexes

$[Cu_4(L^1)_4].0.5(H_2O)$ (1)

A methanolic solution (5 mL) of trimethylamine (1 mmol, 0.101 g) was added dropwise to a methanolic solution (10 mL) of H_2L^1 (1 mmol, 0.193 g) in stirring condition. To this mixture, dropwise addition of methanolic solution (10 mL) of copper perchlorate hexahydrate (1 mmol; 0.370 g) results a deep green solution. The whole reaction mixture was stirred for 2 hours and filtered. The filtrate was kept in open atmosphere for slow evaporation and green single crystals suitable for X-ray diffraction quality were obtained after a few days. Yield: 78 %. *Anal.*Calc. for

$C_{44}H_{52}Cu_4N_4O_{8.50}$ (1027.05): C, 51.45; H, 5.10; N, 5.45 %. Found: C, 51.13; H, 5.13; N, 5.42. IR (cm^{-1}):3430 (vs), 2981 (vw), 1641 (vs), 1553(vs), 1467 (s), 1414 (vs), 1373 (w), 1300 (s), 1195 (vw), 1151 (vw), 1113 (vw), 1078 (s), 1014 (vw), 881(vw), 817 (vw), 763 (vw), 636 (vw).

$[Cu_4(L^2)_2(HL^2)_2(H_2O)_2](sq)\cdot 2(H_2O)$ (2)

A methanolic solution (5 mL) of trimethylamine (1 mmol, 0.101 g) was added dropwise to a solution of H_2L^2 (1 mmol, 0.223 g) under stirring condition. To this mixture, a methanolic solution (10 mL) of copper perchlorate hexahydrate (1 mmol; 0.370 g) was added. To the resulting deep green solution, an aqueous solution of disodium squarate (1 mmol, 0.158 g) was added and stirred for 2 hour, then filtered. Green crystals suitable for X-ray analysis were obtained from the filtrate. Yield: 81%. *Anal.*Calc. for $C_{52}H_{66}Cu_4N_4O_{20}$ (1321.24): C, 47.26; H, 5.03; N, 4.24 %. Found: C, 46.77; H, 4.37; N, 4.11(%). IR (cm^{-1}): 3435 (vs), 2981 (vw), 1642 (vs), 1553(vs), 1466 (s), 1413 (vs), 1373 (s), 1299 (s), 1246 (vw), 1216 (vw) 1078 (s), 1053 (vw), 974(w), 881 (vw), 741 (vw), 640 (vw).

6.2.4 Crystallographic data collection and refinement

X-ray single crystal structural data of compounds **1-2** were collected on a Bruker D8 Venture PHOTON 100 CMOS diffractometer equipped with a INCOATEC micro-focus source operating at 50 kV and 30 mA and graphite monochromated MoKα radiation (λ = 0.71073 Å). The program SAINT [6.10] was used for integration of diffraction profiles and absorption correction was applied with SADABS program [6.11]. All the structures were solved by SIR92 [6.12] and refined by full matrix least-square method using SHELXL-2014/7 [6.13] implemented in WinGX system (ver 2013.3) [6.14]. Three ethyl groups in **1** and two in complex **2** were found disordered over two positions and the occupancies were refined. In addition residuals in all unit cells were interpreted as lattice water molecules that count for 0.5 and 2 1 in complex **1** and **2**,

respectively. All non-H atoms were refined anisotropically. All the hydrogen atoms were fixed at geometrical positions (except those of OH groups and coordinated water molecules in **2** which were located on the difference Fourier map) and included in the final cycles of refinement. Packing diagrams were done with graphical program Diamond [6.15]. Crystallographic and details of structure refinement are given in Table 6.1. The cif file CCDC numbers are 1828395 and 1828396 for complex **1** and **2**, respectively.

Table 6.1 Crystal data and details of structure refinement of complexes.

Complex	**1**	**2**
Empirical formula	$C_{44}H_{52}Cu_4N_4O_{8.50}$	$C_{52}H_{66}Cu_4N_4O_{20}$
Formula mass, g mol^{-1}	1027.05	1321.24
Crystal system	Triclinic	Monoclinic
Space group	$P\bar{1}$	$P2_1/n$
a, Å	12.023(5)	15.9727(7)
b, Å	12.682(5)	19.9309(8)
c, Å	15.142(5)	19.0257(8)
α, deg	84.707(5)	90
β, deg	79.368(5)	102.925(2)
γ, deg	79.585(5)	90
V, $Å^3$	2227.6(15)	5903.4(4)
Z	2	4
$D_{(calcd)}$, g cm^{-3}	1.531	1.487
μ(Mo-Kα), mm^{-1}	1.940	1.497
F(000)	1056	2728
theta range, deg	2.1-27.9	2.1-27.9
No. of collected data	104039	234280
No. of unique data	10617	14068
R_{int}	0.055	0.041
Observed reflns [$I > 2\sigma(I)$]	7292	11495
Goodness of fit (F^2)	1.065	1.069
Parameters refined	571	772
*R*1, *wR*2 ($I > 2\sigma(I)$) [a]	0.0414, 0.0982	0.0447, 0.1279
Residuals, e $Å^{-3}$	-0.340, 0.691	-0.511, 0.895

[a] $R1(Fo) = \Sigma \big| |Fo| - |Fc| \big| / \Sigma |Fo|$, $wR2(Fo^2) = [\Sigma w (Fo^2 - Fc^2)^2 / \Sigma w (Fo^2)^2]^{½}$

6.2.5 Protein binding studies

Stock solutions of human serum albumin (HSA) and bovine serum albumin (BSA) were prepared in HEPES buffer (pH 7.2) solution. Aqueous solutions of complexes were prepared by dissolving the compounds in water: HEPES buffer (1:99). The absorption titration experiments were carried out by keeping the concentration of serum albumins constant (4.75×10^{-5} M for BSA and 3.33×10^{-5} M for HSA), while varying the concentrations of Cu(II) complexes (0 to 11.2 μM). The interactions of compounds with serum albumins were studied by recording the tryptophan fluorescence of BSA / HSA. To the solutions of serum albumin, Cu(II) complexes were added at room temperature, and the quenching of emission intensities at 340 nm (λ_{ex}, 280 nm) for BSA and 330 (λ_{ex}, 280 nm) for HSA were recorded after gradual addition of (20 μL, 0.3475 mmol) aqueous solution of complexes. The Stern-Volmer constant (K_{sv}) and quenching rate constant (k_q) were calculated using the equations $F_0/F = 1 + K_{sv}[complex]$ and $K_{sv} = k_q\tau_0$, where F_0 and F are the fluorescence intensities in the absence and in the presence of the complex, and τ_0 is the fluorescence lifetime of serum albumin (~ 5×10^{-9} s) [6.16]. The binding constant (K_{bin}) and the number of binding sites (n) are calculated using the following Scatchard equation [6.17].

$$\log[(F_o - F)/F] = \log K_{bin} + n \log[complex]$$

6.2.6 DNA binding studies

Electronic absorption spectral study

The binding of complexes with CT-DNA were studied by electronic absorption spectroscopic technique to investigate the possible DNA-binding modes and to calculate the intrinsic binding constant (K_{ib}) for the interaction of the compounds with CT-DNA. For electronic absorption spectral titration, the UV-vis absorption spectra of complexes (5 μM) were recorded with gradual

addition of 20 µL, 0.3059 mmol CT-DNA solution. Intrinsic binding constant (K_{ib}) of the complex with CT-DNA was determined using the equation [6.18]

$$\frac{[DNA]}{(\varepsilon_a - \varepsilon_f)} = \frac{[DNA]}{(\varepsilon_b - \varepsilon_f)} + \frac{1}{K_{ib}(\varepsilon_b - \varepsilon_f)}$$

Where [DNA] is the concentration of CT-DNA, ε_a is the extinction co-efficient value of the complex at a given CT-DNA concentration, ε_f and ε_b are the extinction co-efficient of the complex only and when fully bound to CT-DNA, respectively. The plot of [DNA]/($\varepsilon_a - \varepsilon_f$) vs [DNA] gives a straight line with $\frac{1}{(\varepsilon_b - \varepsilon_f)}$ and $\frac{1}{K_{ib}(\varepsilon_b - \varepsilon_f)}$ as slope and intercept, respectively. From the ratio of the slope to the intercept, the value of K_{ib} was calculated.

Competitive binding fluorescence measurement

The competitive binding nature of ethidium bromide (EB = 3, 8-diamino-5-ethyl-6-phenyl phenanthridinium bromide) and copper(II) compounds, with CT-DNA were studied adopting fluorometric method. In presence of CT-DNA, EB exhibits fluorescence (λ_{em} = 602 nm, λ_{ex} = 500 nm) enhancement due to its intercalative binding to CT-DNA. Gradual addition of copper(II) complexes (20µL, 0.3475 mmol) to aqueous solution (5 µM) of EB bound CT-DNA in HEPES buffer (pH 7.2) results fluorescence quenching due to displacement of EB from CT-DNA. The Stern-Volmer constant (K_{sv}) was calculated using Stern-Volmer equation [6.9] $F_0/F = 1 + K_{sv}[complex]$, where F_0 and F are the emission intensities in absence and in presence of copper(II) compounds, K_{sv} is the Stern-Volmer constant, and [complex] is the concentration of copper (II) complexes.

6.2.7 Molecular docking

DNA-complex docking

We have used HEX 6.3 program to study the DNA-complex interaction. B-DNA dodecamer d(CGCGAATTCGCG)$_2$ (PDB ID: 1bna) (http://www.rcsb.org./pdb) was used as a model compound for CT-DNA [6.19]. X-ray crystal structures of the complexes were used as received from X-ray single crystal data. Spherical polar Fourier correlations were used to perform docking. The following parameters are used for docking: correlation type - shape only, FFT mode - 3D, grid dimension - 0.6, receptor range - 180, ligand range - 180, twist range - 360, distance range - 40. PyMol software was used for visualization of the docked pose.

Serum albumin-complex docking

The AutoDock4.2 [6.20] software was used to perform SAs-complex docking. We used crystal structure of BSA (PDB ID: 4f5s) and HSA (PDB ID: 1ao6), downloaded from protein data bank (http://www.rcsb.org/pdb), for docking. The Chimera program (http://www.cgl.ucsf.edu/chimera/) was used for receptor preparation. During docking calculation, the SAs were kept rigid and complexes being docked were kept flexible. The docking results were visualized by Chimera (http://www.cgl.ucsf.edu/chimera/) and PyMol software.

6.3 Results and discussion

6.3.1 Synthesis aspects

The multisite coordinating ligands H_2L^1 and H_2L^2 (Scheme 6.1), were prepared by a one pot synthesis employing condensation of the 2-amino-1-butanol and corresponding aldehyde in methanol under reflux condition, and characterized by ^1H and ^{13}C NMR spectra. Using these ligands, complexes **1-2** were synthesized at room temperature.

Scheme 6.1 H_2L^1 and H_2L^2 with their coordination modes in complexes

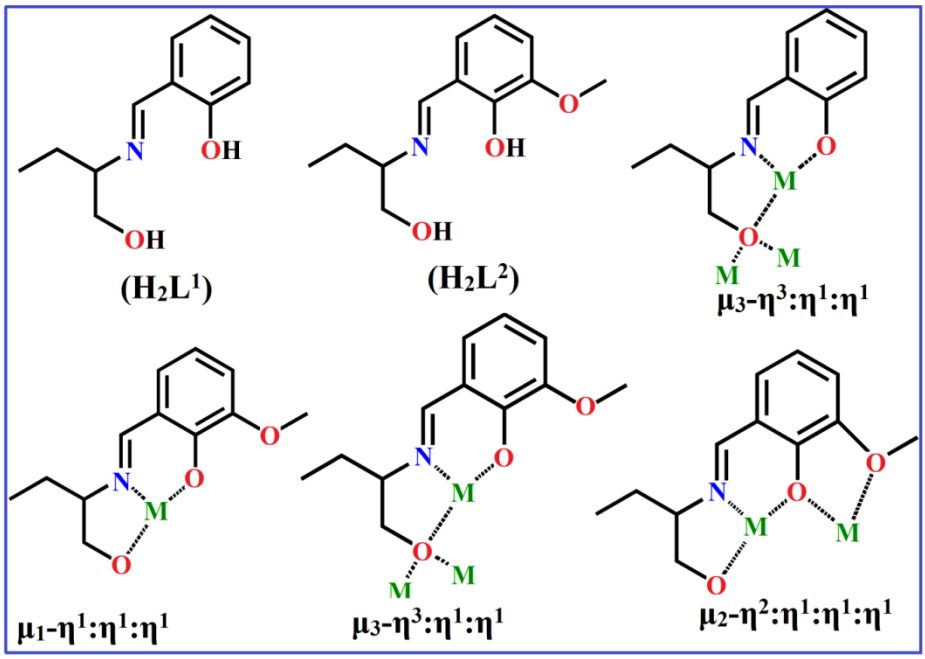

6.3.2 Crystal structure description

$[Cu_4(L1)_4]\cdot 0.5(H_2O)$ (1)

The molecular structure of **1** is shown in Fig. 6.1. Selected bond lengths and angles, and inter-metallic distances are listed in Tables 6.2-6.4. Complex **1** crystallizes in triclinic crystal system with space group $P\bar{1}$ and consists of a tetrameric $[Cu_4(L^1)_4]$ moiety with half lattice water molecule. The tridentate Schiff base ligand (H_2L^1), which can adopt both chelating and bridging modes (Scheme 6.1) undergoes double deprotonation upon addition of triethyl amine (TEA) and the dianionic form of ligand $[(L^1)^{2-}]$, coordinates to the copper(II) centers through the deprotonated alkoxo oxygen, phenolic oxygen and imine nitrogenatomsvia μ_3-η^3:η^1:η^1 coordination mode (Fig. 6.1).

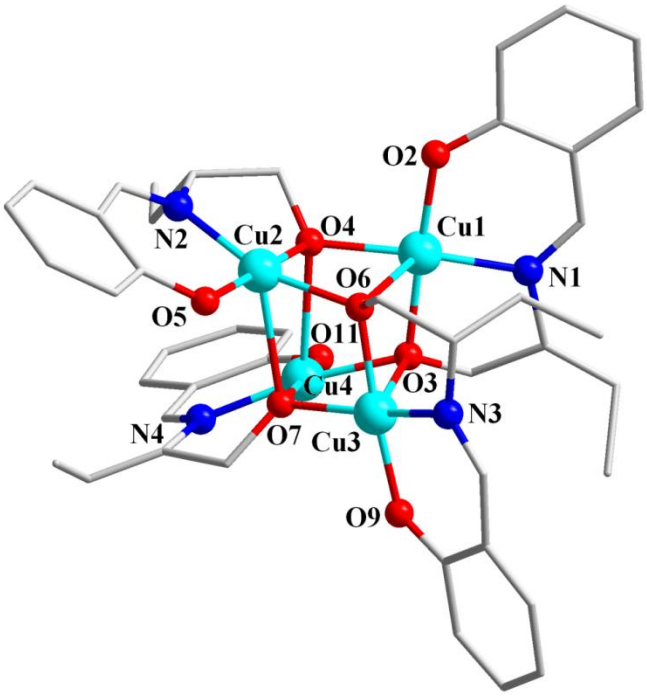

Fig. 6.1. Molecular structure of tetranuclear cubane in **1** with labeling of selected atoms. The lattice water molecule and hydrogen atoms have been omitted for clarity.

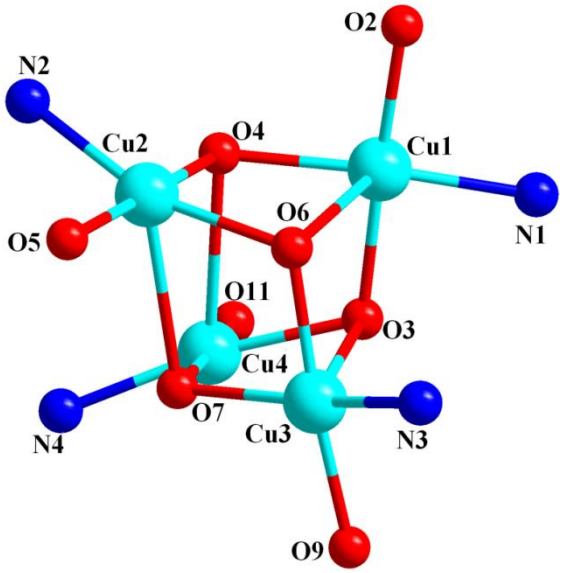

Fig. 6.2. Representation of the tetranuclear copper(II) core in **1** with the coordination environment of metal centers.

The cubane structure is characterized by a Cu_4O_4 core where the anionic alkoxo-oxygen atoms connect three neighboring Cu(II) ions via μ_3-O bridges (Fig. 6.2). The vertices of the cube are occupied by four Cu(II) and four μ_3-bridging alkoxide oxygen atoms in alternating fashion. All Cu(II) centers have five coordination number with NO_4 donor set from the Schiff base ligands. For a penta-coordinated metal center, the distortion of the coordination environment from regular trigonal bipyramidal to square pyramidal can be evaluated by the Addison distortion index (τ), defined as $\tau = [(\beta-\gamma)/60]$, where β and γ are the two largest coordination angles around the metal [6.21] (τ is zero for a perfect square pyramid while it becomes unity for an ideal trigonal bipyramidal geometry). The coordination geometry around each Cu(II) center is distorted square pyramidal being the respective τ values ($\tau = 0.207$ for Cu1, $\tau = 0.206$ for Cu2, $\tau = 0.218$ for Cu3 and $\tau = 0.132$ for Cu4).

Table 6.2 Selected bond lengths (Å) for **1-2**.

1		**2**	
Cu(1)-O(2)	1.890(2)	Cu(1)-O(1)	1.991(2)
Cu(1)-O(3)	1.940(2)	Cu(1)-O(2)	2.423(2)
Cu(1)-O(4)	1.945(2)	Cu(1)-O(3)	1.911(2)
Cu(1)-O(6)	2.564(3)	Cu(1)-O(6)	1.951(2)
Cu(1)-N(1)	1.932(3)	Cu(1)-O(13)	2.4908(19)
Cu(2)-O(4)	1.951(2)	Cu(1)-N(2)	1.939(3)
Cu(2)-O(5)	1.884(2)	Cu(2)-O(1)	1.945(2)
Cu(2)-O(6)	1.971(2)	Cu(2)-O(13)	1.9366(18)
Cu(2)-O(7)	2.506(2)	Cu(2)-O(14)	2.309(2)
Cu(2)-N(2)	1.944(3)	Cu(2)-O(19)	1.970(2)
Cu(3)-O(3)	2.577(3)	Cu(2)-N(1)	1.943(3)
Cu(3)-O(6)	1.936(2)	Cu(3)-O(6)	1.939(2)
Cu(3)-O(7)	1.945(2)	Cu(3)-O(7)	1.980(2)
Cu(3)-O(9)	1.895(2)	Cu(3)-O(8)	1.9409(18)
Cu(3)-N(3)	1.932(2)	Cu(3)-O(9)	2.291(3)
Cu(4)-O(3)	1.957(2)	Cu(3)-N(3)	1.942(3)
Cu(4)-O(4)	2.608(2)	Cu(4)-O(6)	2.509(2)
Cu(4)-O(7)	1.926(2)	Cu(4)-O(8)	2.0116(19)
Cu(4)-O(11)	1.883(3)	Cu(4)-O(10)	2.384(2)
Cu(4)-N(4)	1.943(3)	Cu(4)-O(11)	1.902(2)
		Cu(4)-O(13)	1.9496(19)
		Cu(4)-N(4)	1.943(2)

Table 6.3 Inter metallic distances in complexes **1-2**

	1	**2**
Cu(1)-Cu(2)	3.178	3.184
Cu(1)-Cu(3)	3.313	3.403
Cu(1)-Cu(4)	3.251	3.253
Cu(2)-Cu(3)	3.203	3.765
Cu(2)-Cu(4)	3.395	3.346
Cu(3)-Cu(4)	3.175	3.188

The basal plane of the square pyramid is formed by the phenolate oxygen, the imine nitrogen and two μ_3-alkoxide oxygen atoms, while the apical position is occupied by another μ_3-alkoxide oxygen atom. Cu1, Cu2, Cu3 and Cu4 atoms are displaced from the corresponding mean plane by 0.0625, 0.0810, -0.0892 and -0.0719 Å, respectively, towards the apical ligand atom.

Table 6.4 Coordination bond angles [º] for **1 - 2**.

1		**2**	
Cu(1)-O(4)-Cu(2)	109.32(11)	Cu(1)-O(6)-Cu(4)	92.79(8)
Cu(1)-O(3)-Cu(3)	93.28(9)	Cu(3)-O(6)-Cu(4)	90.62(8)
Cu(1)-O(3)-Cu(4)	113.08(11)	Cu(3)-O(8)-Cu(4)	107.51(9)
Cu(1)-O(4)-Cu(4)	89.88(8)	Cu(1)-O(13)-Cu(2)	91.10(7)
Cu(1)-O(6)-Cu(2)	87.98(8)	Cu(1)-O(13)-Cu(4)	93.40(7)
Cu(1)-O(6)-Cu(3)	93.77(9)	Cu(2)-O(13)-Cu(4)	118.84(10)
Cu(2)-O(4)-Cu(4)	95.16(8)	Cu(1)-O(1)-Cu(2)	108.00(9)
Cu(2)-O(6)-Cu(3)	110.09(10)	Cu(1)-O(6)-Cu(3)	122.03(11)
Cu(2)-O(7)-Cu(3)	91.15(8)	Cu(2)-O(8)-Cu(3)	100.80(8)
Cu(2)-O(7)-Cu(4)	99.16(9)	Cu(2)-O(8)-Cu(4)	84.24(7)
Cu(3)-O(3)-Cu(4)	87.79(9)		
Cu(3)-O(7)-Cu(4)	110.17(11)		

The Cu-O and Cu-N bond lengths in the equatorial plane vary from 1.883(3) to 1.971(2) Å and from 1.932(2) to 1.943(3) Å, respectively (Table 6.2). The apical oxygen atoms show longer Cu-O bond lengths in between 2.504(3) - 2.607(3) Å due to the Jahn-Teller distortion of the d^9 copper center. The Schiff base ligand $[(L^1)^{2-}]$ acts as a tridentate for one copper(II) ion leading to five and six-membered chelate rings with average bite angles of 83.83 and 94.01°, respectively. The bridging Cu-O-Cu bond angles are in between 87.79(9)- 113.08(11)° (Table 6.4). Based on Cu...Cu distance (Table 6.3), Cu_4O_4 core can be classified as (4+2) system [6.7].

$[Cu_4(L^2)_2(HL)_2(H_2O)_2]\cdot(Sq)\cdot 2(H_2O)$(2)

The crystal structure of **2** is shown in Fig. 6.3. The compound crystallizes in monoclinic crystal system with space group $P2_1/n$. Selected bond lengths and angles as well as inter-metallic distances are summarized in Tables 6.2-6.4. The core framework of complex **2** possesses double-open cubane structure (Fig. 6.4).

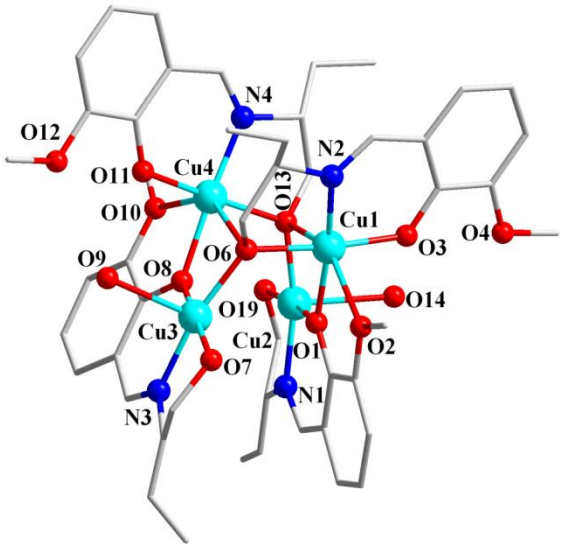

Fig. 6.3. Molecular structure **2** with labeling of selected atoms. The lattice water molecules, lattice squarate anion and hydrogen atoms have been omitted for clarity.

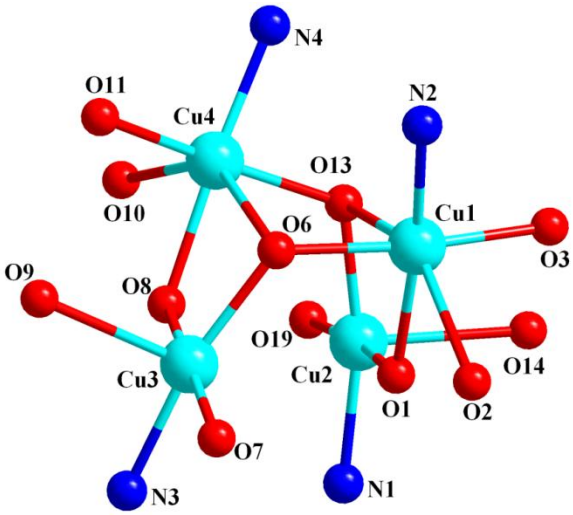

Fig. 6.4. Representation of the tetranuclear copper(II) core in **2** with the coordination environment of the metal centers.

The cationic complex comprises four copper(II) centers, two double deprotonated $[(L^2)^{2-}]$, two monodeprotonated $[(HL^2)^-]$ ligands and two coordinated water molecules. The charge of the cationic complex is counter balanced by a lattice squarate anion. In addition, three residuals were interpreted as lattice water molecules, two of which at half occupancy. Each mono deprotonated $(HL^2)^-$ chelates two copper atoms *via* μ_2-η^2:η^1:η^1:η^1-O,O,N,O coordination mode, while the double deprotonated $(L^2)^{2-}$ chelates Cu1 and Cu4 centers and simultaneously connect to the previous moieties with the μ_3-alkoxido group resulting μ_3-η^3:η^1:η^1-O,N,O coordination mode, and the methoxy oxygen O4 and O12 remain uncoordinated. Fig. 6.4 shows a simplified representation of the coordination environment around the four copper centers. The metal ions Cu2 and Cu3 present a similar square pyramidal (τ = 0.098 for Cu2, τ = 0.094 for Cu3) geometry. The basal plane of the square pyramid is formed by the imine nitrogen (N1 for Cu2; N3 for Cu3), the phenoxido (O1 for Cu2; O8 for Cu3) and the alcoholic oxygen atoms (O19 for Cu2; O7 for Cu3) of $(HL^2)^-$, and completed with the alkoxido oxygen atom (O13 for Cu2; O6 for

Cu3) through μ_3-bridging from a $(L^2)^{2-}$. A water molecule occupies the apical position of the square pyramid. The basal coordination bond distances for Cu2 and Cu3 (Table 6.2) are in between 1.937(18)-1.980(2) Å, while the Cu-OH_2 bond lengths are somewhat more distant, being of 2.309(2) and 2.291(3) Å for Cu2 and Cu3, respectively (Table 6.2).

The coordination environment of Cu1 and Cu4 are also identical, both the metal centers exhibit a distorted octahedral geometry. The equatorial plane of the octahedron is formed by the imine nitrogen, the phenoxido and the alkoxido oxygen from one $(L^2)^{2-}$ ligand and μ_2-phenoxido oxygen of $(HL^2)^-$, the axial positions are occupied by the methoxy oxygen of same $(HL^2)^-$ and the alkoxido oxygen atom of another $(L^2)^{2-}$ ligand.

The equatorial bond distances fall in the range 1.902(2)-2.012(19) Å, while the axial bond lengths vary from 2.384(2) to 2.509(2) Å, due to the Jahn-Teller distortion. The Cu2-O8 (2.883 Å) and Cu3-O1 (2.985 Å) distances are rather long and responsible for the double open cubane core structure. The metal atoms are located at the vertices of a distorted tetrahedron with edge dimension varying from 3.184(6) to 3.765(5) Å. Based on Cu...Cu distances, (Table 6.3) complex **2** also belong to class (4+2) copper cubane system.

6.3.3 Electronic absorption and emission spectra of complexes

The electronic spectra of complexes **1** and **2** were recorded in methanol. The spectrum of **1** (Fig. 6.5) shows significant transitions at 215 nm ($\varepsilon \sim 8.4 \times 10^4$ liter $mole^{-1}$ cm^{-1}), 238 nm ($\varepsilon \sim 5.6 \times 10^4$ liter $mole^{-1}$ cm^{-1}), 258 nm ($\varepsilon \sim 4.6 \times 10^4$ liter $mole^{-1}$ cm^{-1}) and 343 nm ($\varepsilon \sim 1.0 \times 10^4$ liter $mole^{-1}$ cm^{-1}). For the spectrum of **2** (Fig. 6.5) shows transition at 232 nm ($\varepsilon \sim 1.5 \times 10^5$ liter $mole^{-1}$ cm^{-1}), 270 nm ($\varepsilon \sim 1.2 \times 10^5$ liter $mole^{-1}$ cm^{-1}) and 370 nm ($\varepsilon \sim 2.2 \times 10^4$ liter $mole^{-1}$ cm^{-1}). The intense high energy bands around 215-275 nm are observed in free ligands as well as in complexes which have been assigned to the intraligand $\pi \rightarrow \pi^*$ and $n \rightarrow \pi^*$ transitions, these

bands exhibit slight blue and red shift in complexes, indicating the formation of complex. On the other hand bands at 343 nm (for **1**) and 370 nm (for **2**) are charge transfer in origin and can be attributed to the transition from the coordinated ligand to the metal ion (LMCT), in which the lone pair of electrons on the oxygen / nitrogen atom is transferred to the unoccupied d orbital of the Cu^{2+} ions.

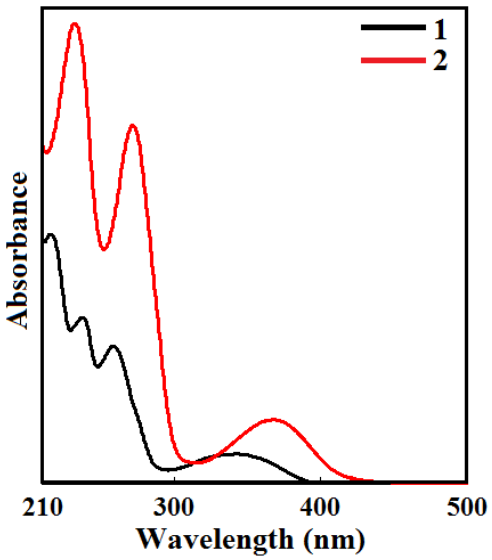

Fig. 6.5 Absorption spectra of complexes **1-2**.

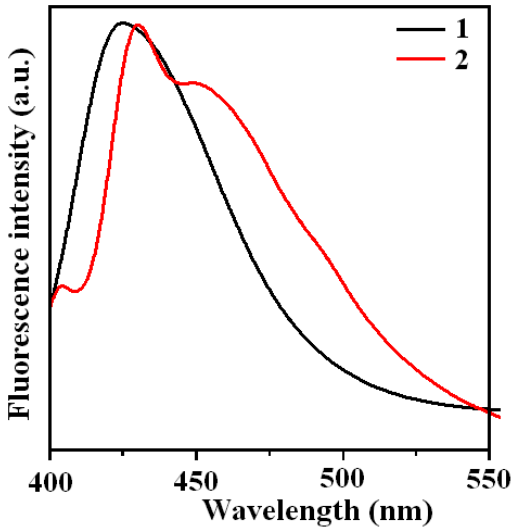

Fig. 6.6 Fluorescence spectra of complexes **1-2**.

Table 6.5 Electronic absorption and emission spectra of complexes.

	Absorption / λ (nm); ε (M^{-1} cm^{-1})	Emission (nm)	$\Delta\nu^a$, nm	Φ_s
1	215 (8.4×10^4), 238 (5.6×10^4), 258 (4.6×10^4),**343** (1.0×10^4)	425	82	0.39
2	232 (1.5×10^5), 270 (1.2×10^5), **370** (2.2×10^4)	404, 430, 451	34, 60, 81	0.51

Bold number indicates the excitation wavelengths. [a]Stoke shift

Results of the study of luminescence properties are summarized in Table 6.5. Both the complexes exhibit red shifted emission. On excitation at 343 nm complex **1** exhibits luminescence bands at 425 nm (Fig. 6.6) with a fluorescence quantum yield Φ_s = 0.39. On the other hand on excitation at 370 nm complex **2** exhibits luminescence bands at 404, 430 and 451 nm (Fig. 6.6) with a quantum yield (Φ_s) = 0.51. As squaric acid show no emission spectra at

room temperature [6.22], the extra luminescence bands of **2** may be due to the presence square pyramidal as well as octahedral coordination environment of copper(II).

6.3.4 **Magnetic properties of complexes**

The $\chi_M T$ versus T curves for complexes **1** and **2** are shown in Fig. 6.7. The $\chi_M T$ versus T curve for complex **1** shows a room temperature value of 1.49 $cm^3mol^{-1}K$, in agreement with the value of 1.48 $cm^3mol^{-1}K$ expected for four uncoupled S = ½ spins assuming g = 2, and it decreases continuously until reaching a value of 0.18 $cm^3mol^{-1}K$ at 10 K. Below this temperature and down to 5 K, the $\chi_M T$ value decreases smoothly, showing the tendency to form a plateau at a value between 0.18 and 0.16 $cm^3mol^{-1}K$. Below 5 K, the curve drops further and faster down to a value of 0.14 $cm^3mol^{-1}K$ at 2 K.

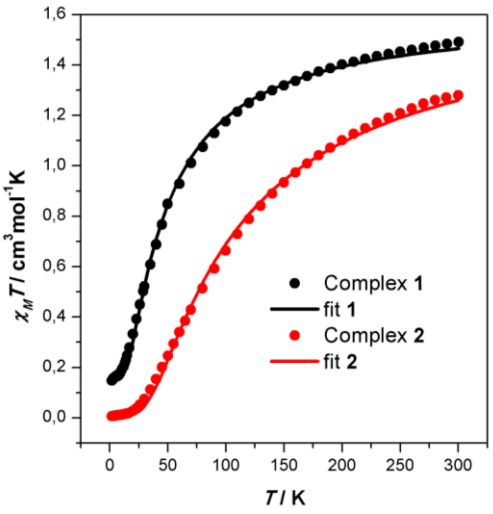

Fig. 6.7. Thermal dependence of the $\chi_M T$ for complexes **1** and **2**. The solid lines are the fits obtained considering the models of Fig. 6.8 and using the Hamiltonian and parameters mentioned in the text.

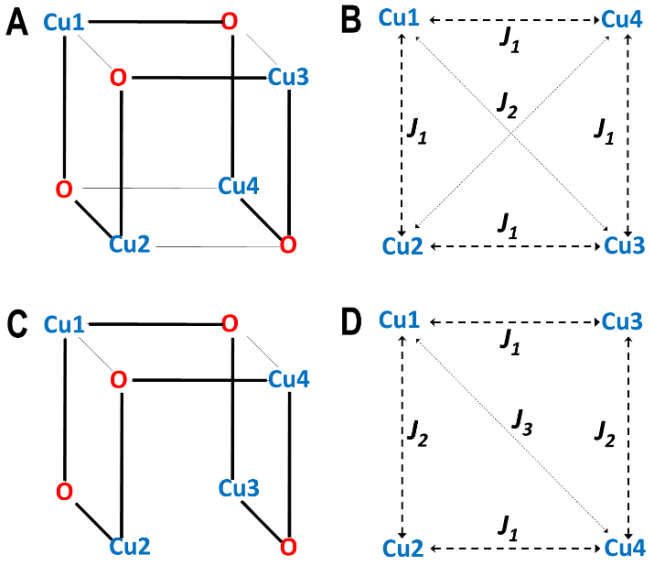

Fig. 6.8 A) Structural arrangement of a [4+2] cubane structure as that of complex **1** and C) of a [4+2] double-open cubane structure as that of complex **2**: short (equatorial) and long (axial) Cu-O bonds are illustrated with thick and thin lines, respectively. B, D) Exchange coupling models used for the magnetic analysis of complexes **1** and **2**, respectively.

On the other hand, the $\chi_M T$ versus T curve for complex **2** shows a room temperature value of 1.28 $cm^3mol^{-1}K$, slightly lower than the value expected for four uncoupled S = ½ spins assuming g = 2, and it decreases continuously down to 25 K, forming a sort of plateau at a value close to 0 below this temperature. This behavior evidences an overall antiferromagnetic interaction in both complexes, and suggests the presence of impurities with a spin different than 0, resulting in the formation of the plateau (Fig. 6.7) in the $\chi_M T$ versus T curves at values different from 0.

Complex **1** presents a cubane-like structure characterized by a $[Cu_4O_4]$ core that possesses four short and two long Cu···Cu distances as a result of the particular relative arrangement of the axial axes and equatorial planes of the Cu(II) ions, leading to a [4+2] geometric type of cubane compounds proposed by Ruiz et al [6.7]. The corresponding equatorial or axial character of the bridging atoms with respect to the two connected Cu(II) ions in each pair is shown in Fig. 6.8A. Taking account of this structural arrangement, the magnetic behavior of the complex can be

studied by employing the isotropic spin Hamiltonian of equation 1, based on the model of Scheme 6.8B.

$$H = -J_1 (S_1S_2 + S_1S_4 + S_2S_3 + S_3S_4) - J_2 (S_1S_3 + S_2S_4) \quad \text{eq. 1}$$

J_1 describes the magnetic exchange coupling between the four Cu(II) pairs with short Cu···Cu distances, while J_2 characterizes the magnetic exchange coupling between the remaining two Cu(II) pairs with long Cu···Cu distances. The $\chi_M T$ vs T curve of complex **1** was fitted with the PHI program [6.23]. Although the four Cu(II) ions are not equivalent in the crystal, the same g value was assigned to all of them after considering their similarities. For the spin Hamiltonian described in equation 1, a good agreement with the experimental curve was found with the following parameters: g = 2.14, J_1 = -20.2 cm^{-1} and J_2 = -1.7 cm^{-1}. In addition, 15% of impurities with an S = 1 ground state had to be also considered in order to fairly reproduce the experimental data. The presence of such impurities is most likely due to the co-crystallization of ferromagnetic Cu(II) dimeric species with complex **1**. Temperature-independent paramagnetism (TIP) was considered equal to 120 × 10^{-6} cm^3mol^{-1}. The fitted curve is represented together with the experimental one in Fig. 6.7. The results of the fit are in agreement with orbital symmetry considerations and previously reported correlations: the Cu(II) pairs with short Cu···Cu distances are bridged by two different O atoms, of which one of them provides an exchange pathway formed exclusively by magnetic orbitals of both Cu(II) ions in the pair, leading to a significant antiferromagnetic interaction due to an efficient orbital overlap. On the contrary, Cu(II) pairs characterized by a long Cu···Cu distance always involve a non-magnetic orbital in any of their bridging pathways, and consequently the interaction is much weaker in these cases. Thus, J_1 is expected to be more negative than J_2 in [4+2] cubane systems, as observed experimentally. In addition, and according to the work of Tercero *et al.* [6.24], the sign and magnitude of the J_1

magnetic exchange constant in [4+2] type of cubane compounds should correlate with the Cu-O-Cu angle characteristic of the short exchange pathway made exclusively by magnetic orbitals. In fact, calculations suggest that antiferromagnetic interactions can be expected in $[Cu_4O_4]$ compounds with angles larger than ca. 103°, so that the overlapping of magnetic orbitals becomes effective. This correlation justifies the results obtained for complex **1**, being the value of the J_1 magnetic exchange constant equal to -20.2 cm^{-1}, in agreement with a range of θ values between 109 and 113° in the magnetic core of the complex.

Complex **2** belongs to a specific type of [4+2] cubane compound where one of the two long Cu···Cu distances is formed by a Cu(II)-Cu(II) pair not connected through a bridging ligand, and thus their magnetic exchange can be neglected. These types of core systems are known as double-open cubane structures. Their structural arrangement and their corresponding equatorial or axial character of the bridging atoms with respect to the two connected Cu(II) ions in each pair is shown in Fig. 6.8C. Based on this, the magnetic behavior of the complex can be studied by employing the isotropic spin Hamiltonian of equation 2, which derives from the model, showed in Scheme 8D.

$$H = -J_1 (S_1S_3 + S_2S_4) - J_2 (S_1S_2 + S_3S_4) - J_3S_1S_4 \qquad \text{eq. 2}$$

In this case, and due to the particular double-open structure that forces a different coordination number and environment in the four Cu(II) ions, the latter can no longer be considered magnetically equivalent as in the case of complex **1**, and as consequence the magnetic exchange coupling characteristic of the four short Cu···Cu distances is split into two clearly different constants, here described by J_1 and J_2.J_3 instead describes the magnetic exchange established through the only Cu(II)-Cu(II) bridged pair showing long distance.

The $\chi_M T$ vs T curve of complex **2** was fitted with the PHI program [6.23]. In this case, two g values were considered in the analysis: one for the octahedral Cu1 and Cu4 ions and one for the Cu2 and Cu3 ions exhibiting a square based pyramid geometry. In order to avoid over-parametrization in the analysis, J_3 was assumed to be null, which seems reasonable considering the magnetic results and symmetry considerations described regarding the analogous J_2 of complex **1**. For the spin Hamiltonian described in equation 2, a good agreement with the experimental curve was found with the following parameters: g_1 = 2.14, g_2 = 2.12, J_1 = -54.8 cm^{-1}, J_2 = -15.9 cm^{-1} and J_3 = 0 cm^{-1} for complex **2**. In addition the fit was improved by considering the presence of a 3% Cu(II) mononuclear impurity. Temperature-independent paramagnetism (TIP) was considered equal to 120 × 10^{-6} $cm^3 mol^{-1}$. The fitted curve is represented together with the experimental one in Fig. 6.7. As in the case of complex **1**, the sign and magnitude of J_1 and J_2 magnetic exchange constants in complex **2** should correlate with the corresponding Cu-O-Cu angles formed exclusively by equatorial Cu-O bonds. The value of this angle determines the degree of overlapping between the two magnetic orbitals of the Cu(II) ions in the pair, and thus it is critical in determining the exchange constant value. In the complexes reported in this work, the largest antiferromagnetic constant J_1 describes the magnetic coupling in two Cu(II) pairs that show large Cu-O-Cu angles of 118.84 and 122.03°. The other two Cu(II) pairs show smaller Cu-O-Cu angles of 107.51 and 108.00°, and the magnetic analysis indicates an overall weaker antiferromagnetic interaction in this case, with the J_2 constant much smaller than J_1. As expected from the magneto-structural correlation reported by Tercero *et al.* [6.24], the larger the Cu-O-Cu angle, the stronger the antiferromagnetic coupling in the pair. Additionally, the antiferromagnetic nature of the two constants agrees well with the reported crossover angle of 103°, below which a

ferromagnetic exchange would be operative, as observed by some of us in a previous work, as well as by some other authors [6.25].

6.3.5 Protein binding studies

Absorption spectral studies

The UV-vis absorption spectral study offers a simple way to explore the type of interaction of complex with the serum albumins. UV-visible absorption spectra of serum albumins in the absence and presence of the complexes (Fig. 6.9) show that the absorption intensity of BSA / HSA were enhanced with a little blue shift (8 nm, 11 nm for **1**; 7 nm, 6 nm for **2**, respectively) as the complexes were added (up to 13.36 μM).

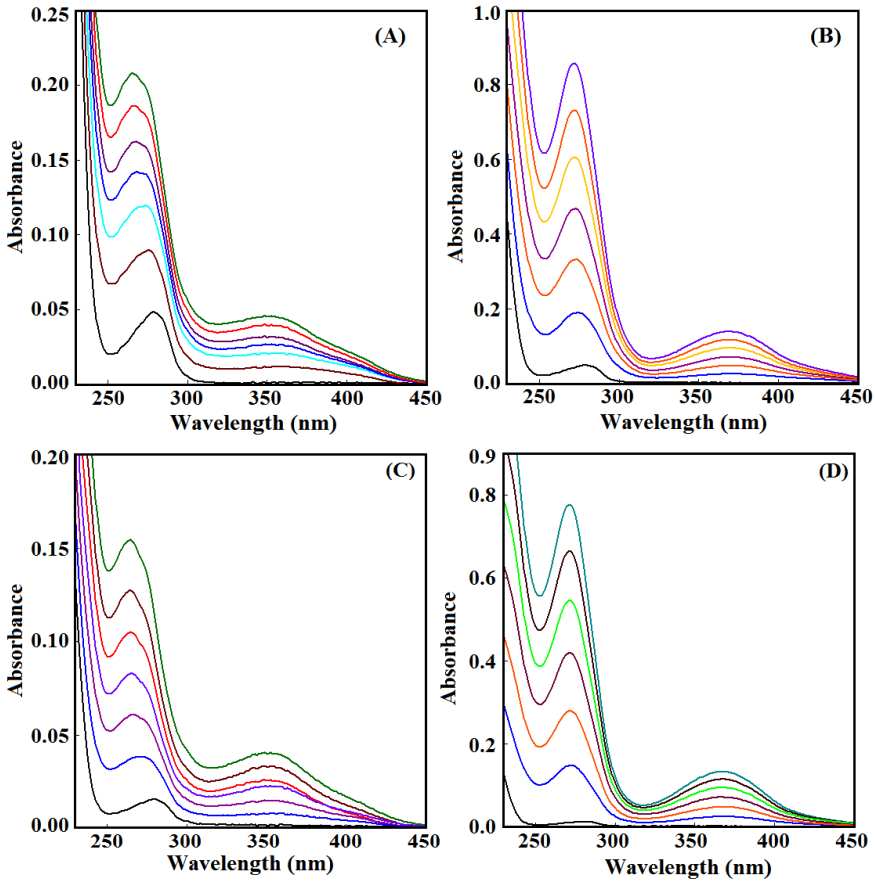

Fig. 6.10 Change of electronic absorption spectra of BSA (A for **1**; B for **2**) and HSA (C for **1**; D for **2**) upon gradual addition of complexes **1**-**2** at temperature 300 K.

The apparent association constant (K_a) were calculated (Fig. 6.10) using the following equation.

$$\frac{1}{(A_{obs} - A_0)} = \frac{1}{(A_c - A_0)} + \frac{1}{K_a(A_c - A_0)[complex]}$$

Table 6.6 Quenching Constant (K_q), binding Constant (K_{bin}), number of binding sites (n) and apparent association constant (K_a) for the interactions of complexes with BSA and HSA.

	Complexes	$K_{sv}(M^{-1})$	$k_q(M^{-1}S^{-1})$	K_{bin} (M^{-1})	n	$K_a(M^{-1})$
BSA	**1**	1.50×10^5	3.00×10^{13}	5.99×10^4	1.37	2.23×10^3
	2	7.76×10^5	1.55×10^{14}	1.48×10^5	1.61	2.28×10^4
HSA	**1**	1.46×10^5	2.92×10^{13}	1.23×10^5	0.99	3.03×10^3
	2	1.86×10^5	3.72×10^{13}	1.48×10^5	1.15	6.62×10^3

The plot of 1 / [complex] vs 1 / (A_{obs} - A_0) gives a straight line (Fig. 7S). From the ratio of the intercept to the slope the values of K_a were calculated and the apparent association constants (K_a) 2.23×10^3 (for **1**-BSA), 3.03×10^3 (for **1**-HSA), 2.28×10^3 (for **2**-BSA) and 6.62×10^3 (for **2**-HSA) Table 6.6. These values indicate that all the complexes have comparable binding affinity.

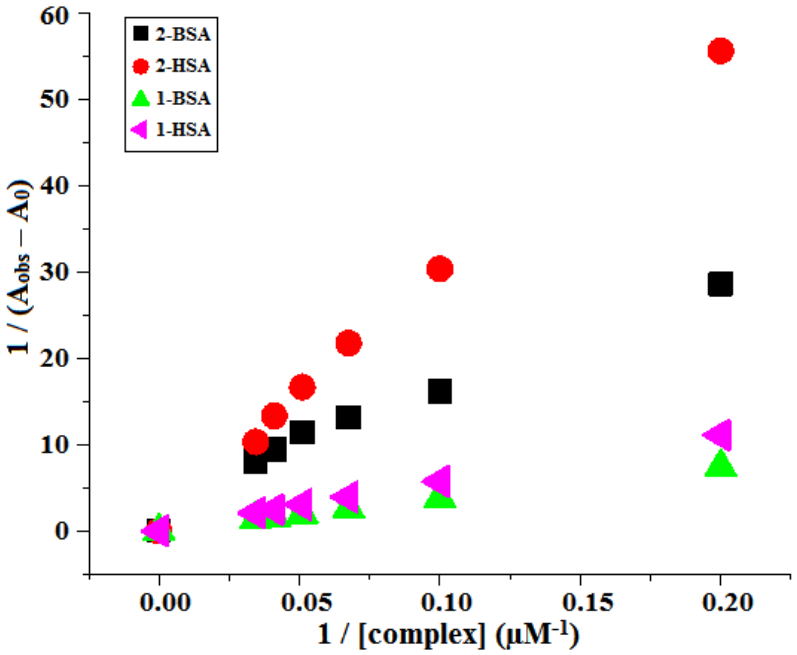

Fig. 6.10 Plot of 1/[complex] vs 1/ (A_{obs}-A_0) for the calculation of apparent association constant (K_a).

Fluorescence spectroscopic studies

The emission spectrum of SAs arises due to presence of tryptophan and tyrosine residues and an alternation in the emission spectra occurs primarily from the tryptophan residue due to changes in protein conformational, subunit association, substrate binding or denaturation [6.26]. Therefore, changes in emission spectral of SAs in presence of complexes can provide important information about the structure, dynamics and protein folding. Fluorescence titration experiments have been performed at room temperature using fixed concentration of SAs (0.475 µM BSA and 0.333 µM HSA) and varying the concentration of complexes (0-11.2 µM) in the wavelength range 290-500 nm (λ_{ex}= 280 nm). The change of fluorescence spectra of SAs upon gradual addition of 20 µL, 0.3475 mm solution of complexes are shown in Fig. 6.11.

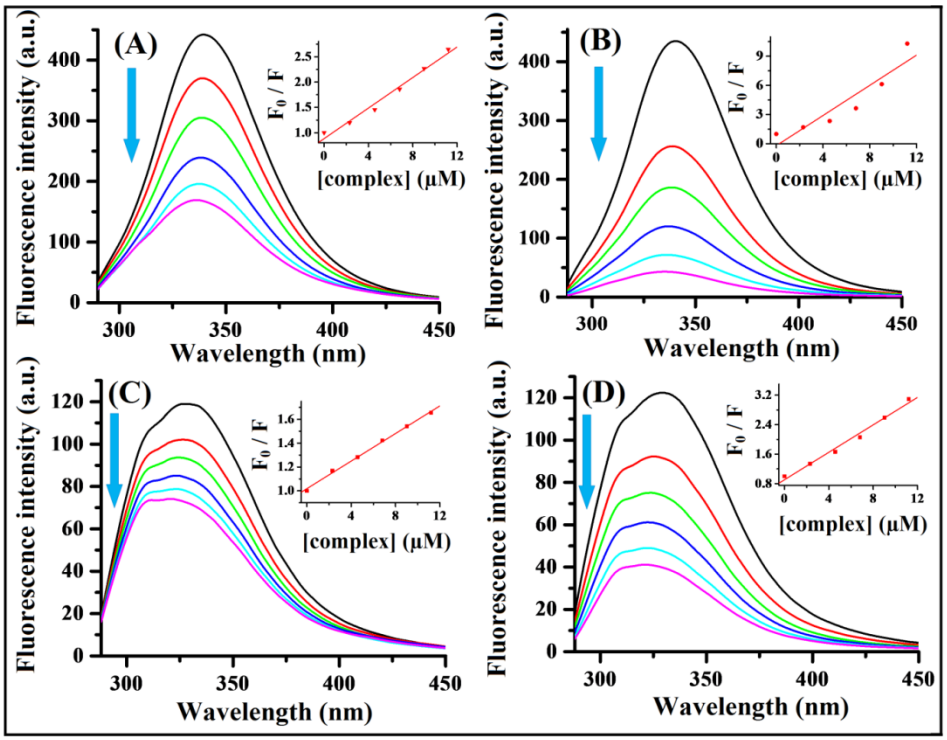

Fig. 6.11 Emission spectrum of BSA (λ_{ex} = 280 nm; λ_{em} = 340 nm) and HSA (λ_{ex} = 280 nm; λ_{em} = 330 nm) in the presence of increasing amounts (0 - 11.2 µM) of complexes **1** (A, C) and **2** (B, D). Arrow shows that the emission intensity changes upon increasing complex concentration. Inset: Stern-Volmer plot.

The fluorescence intensity of BSA (at ~340 nm) quenched (62.17 % for **1** and 90.28 % for **2**) with a small hypsochromic shift (3 nm for **1** and 4 nm for **2**). The emission band of HSA (at ~330 nm) also quenched (39.58 % for **1** and 67.70 % for **2**) with blue shift (6 nm for **1** and 7 nm for **2**). Hypsochromic shift of emission spectral bands indicate that both the complexes bind with the serum albumins and the active site of protein become hydrophobic in presence of complexes [6.27].

From the Stern-Volmer plot [6.9] a linear relationship were obtained for the titration of serum albumins using complexes as a quencher (inset of Fig. 6.11). The calculated values of Stern-Volmer constants (K_{SV}) and quenching rate constant (K_q) for BSA binding are $K_{SV} = 1.50\times10^5$, $K_q = 3.00\times10^{13}$ for **1** and $K_{SV} = 7.76\times10^5$, $K_q = 1.55\times10^{14}$ for **2**. Whereas for HSA binding $K_{SV} = 1.46\times10^5$, $K_q = 2.92\times10^{13}$ for **1** and $K_{SV} = 1.86\times10^5$, $K_q = 3.72\times10^{13}$ for **2** (Table 6.6). The K_q values are 1000 fold higher than the maximum optical collision constant (2×10^{10} $M^{-1}S^{-1}$) of various kinds of quenchers to biopolymers. This suggested that quenching of SAs in presence of copper(II) complexes is occurs via a static quenching mechanism [6.28]. The occurrence of static quenching also supported by the change of UV-vis absorptions spectra of serum albumins in presence of complexes.

As both the complexes bind with SAs in a static mode, the equilibrium binding constant (K_{bin}) and number of binding site (n) were calculated from the plot of log $[(F_o - F)/F]$ versus log [complex] (Fig. 6.12) using the Scatchard equation [6.17]. Calculated values of binding constant (K_{bin}) are 5.99×10^4 M^{-1} (for **1**-BSA), 1.48×10^5 M^{-1} (for **2**-BSA), 1.23×10^5 M^{-1} (for **1**-HSA), 1.48×10^5 M^{-1} (for **2**-HSA) and the number of binding sites per albumin (n) for the complexes are 1.37 (for **1**-BSA), 1.61 (for **2**-BSA), 0.99 (for **1**-HSA) and 1.15 (for **2**-HSA) (Table 6.6).

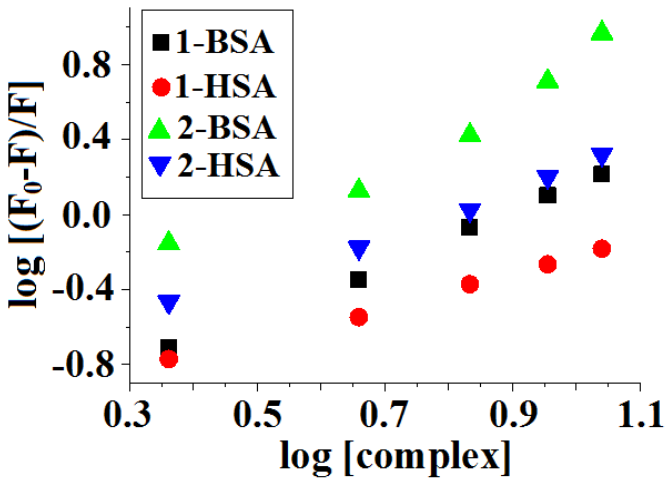

Fig. 6.12 Scatchard plots of the SAs fluorescence titration for complexes **1-2**.

6.3.6 Interaction with Calf-Thymus DNA

Transition metal complexes bind to double-stranded DNA through covalent or non-covalent interactions. Non-covalent interactions with DNA occur through three types of binding modes: electrostatic interactions, intercalative binding and groove binding [6.29]. The interactions of complexes with calf thymus DNA (CT-DNA) were investigated with Uv-vis absorption and fluorescence methods.

Absorbance spectral studies

Electronic absorption spectral studies have been performed to observe the mode of interaction of complexes with CT-DNA. Usually intercalation between the metal complexes and DNA results in hypochromism with or without red / blue shift, on the other hand non-intercalative / electrostatic interaction cause hyperchromism [6.30].

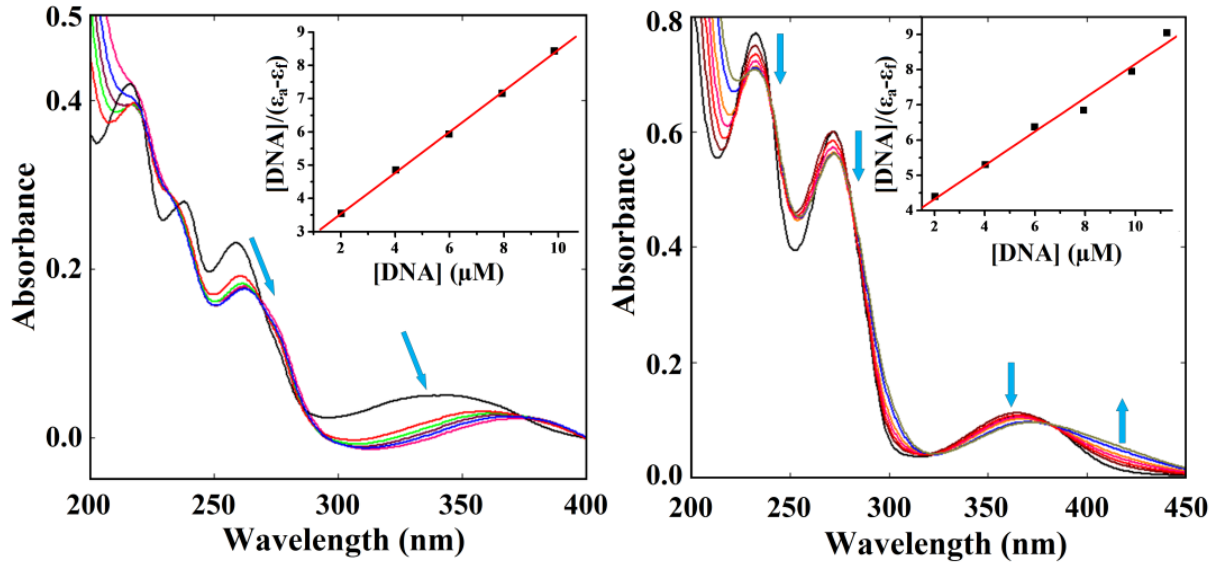

Fig. 6.13 Absorption titration spectra of complexes **1** (left) and **2** (right) in the absence (black line) and presence (other lines) of CT-DNA to complex at room temperature. Inset: Plot of [DNA]/(ε_a-ε_f) versus [DNA]. Arrow shows the absorbance changes upon increasing CT-DNA concentration.

The absorption spectra of the complexes in the absence and presence of CT-DNA are shown in Fig. 6.13. Gradual addition of CT-DNA (20 µL, 0.3059 mmol), to the 5 µM, 3 mL solution of complexes results decrease in absorption intensity (hypochromism) (25 % for **1** and 9 % for **2**) with a significant red shift (4 nm for **1** and 1 nm for **2**). This observation suggests that the complexes bind to CT-DNA with intercalation mode. The plots of [DNA] / (ε_a-ε_f) versus [DNA] give straight lines (inset of Fig. 6.13), and the intrinsic binding constant (K_{ib}) were calculated from the ratio of the slopes to the intercepts. Calculated values of intrinsic binding constants (K_{ib}) are 1.40×10^5 and 2.61×10^5 M^{-1} (Table 6.7) for complexes **1** and **2**, respectively. The values of binding constant suggest that both the complexes strongly bind with CT-DNA and have comparable binding affinity.

Competitive binding between Ethidium Bromide and Compounds

CT-DNA bounded EB shows emission at 602 nm on excitation at 500 nm and addition of a metal complex which is capable to bind CT-DNA via intercalation could result in a quenching emission due to the displacement of EB from CT-DNA-EB system by the complex. The emission spectra of EB bound CT-DNA in the absence and presences of complexes are shown in Fig. 6.14. Gradual addition of copper complexes (20 µL, 0.3475 mmol) to aqueous solution (5 µM, 3 mL) of EB bound CT-DNA (in HEPES buffer, pH 7.2) results quenching of the emission of EB bounded CT-DNA. The emission bands exhibited hypochromism up to 51 % and 62 % for **1**, and **2**, respectively. Observed decrease in emission intensity indicate that the EB molecules are displaced from the CT-DNA binding sites by complexes [6.31]. From the Stern-Volmer plots (inset of Fig. 6.14), straight lines (R = 0.99) were obtained.

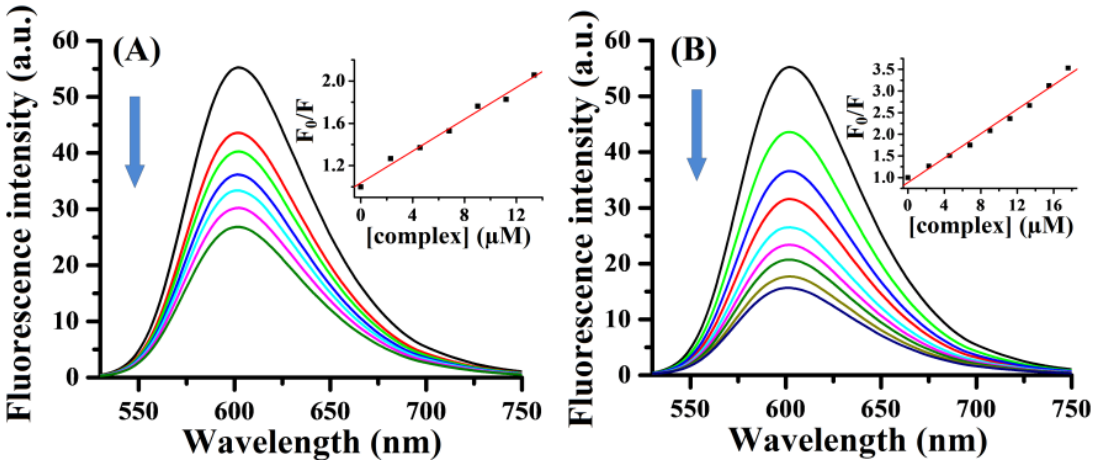

Fig. 6.14 Emission spectra of EB bounded CT-DNA in the presence of complex **1** (A) and **2** (B). Inset: Stern-Volmer plot of fluorescence titrations.

Calculated values of Stern-Volmer constants (K_{sv}) are 0.79 × 10^5, 1.40 × 10^5 and 0.75 × 10^5 M^{-1} for **1**, **2** and **3**, respectively. The apparent DNA binding constant (K_{app}) values were also calculated using the equation [6.32]:

$$K_{EB}[EB] = K_{app}[complex]$$

Where [complex] is the complex concentration value at a 50 % reduction in the fluorescence intensity of EB, K_{EB} (1.0×10^7 M^{-1}) is the DNA binding constant of EB and [EB] is the concentration of EB (5 μM). The calculated values of K_{app} are 3.74×10^6 and 5.54×10^6 M^{-1} for **1** and **2**, respectively (Table 6.7). These results indicate that all the complexes have comparable binding affinity and in agreement with the results obtained from the UV-vis spectral studies.

Table 6.7 Emission and absorption spectral parameters of the Cu(II) complexes bound to CT-DNA.

	λ_{max} (nm)	change of in emission	Δε (%)	$K_{sv}(M^{-1})$	K_{app} (M^{-1})	K_{ib} (M^{-1})	Free energy of interaction (Kcal/mole)
1	602	hypochromism	51.52	0.79×10^5	3.74×10^6	1.40×10^5	-336.6
2	602	hypochromism	62.48	1.40×10^5	5.54×10^6	2.61×10^5	-338.5

6.3.7 Molecular docking

Molecular Docking with DNA

Molecular docking techniques are an important tool to understand the DNA-drug interactions in rational drug design and as well as in the mechanistic study by placing a small molecule into the binding site of the target specific region of the DNA mainly in a non-covalent fashion [6.33]. Molecular docking have been performed on B-DNA (PDB ID: 1bna) in presence of complexes **1** and **2**. Fig. 6.15 exhibits minimum energy conformation of complexes.

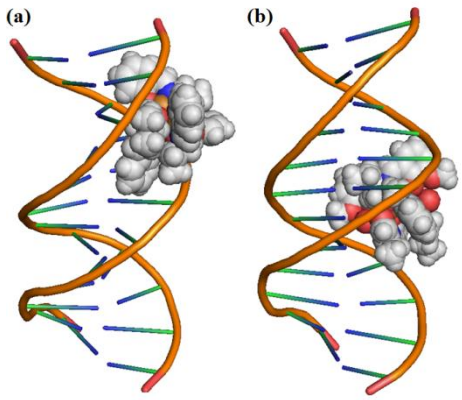

Fig. 6.15 Molecular docked model of complexes **1** (a) and **2** (b) with DNA (PDB ID: 1BNA)

The minimum energy structures indicate that all the complexes are sitting in the major groove of B-DNA with a relative binding energy of -336.6 (**1**) and -338.5 (**2**) Kcal/mole, respectively (Table 6.7). The binding free energy of docked complexes suggests that both the complexes spontaneously bind with DNA and the binding affinities of complexes are comparable. The UV-vis spectroscopic study of complexes show hypochromic shifts of absorption spectral bands which indicate that the interaction may occur with intercalation or groove binding. The docking result clearly confirm that the interaction occur through groove binding.

Molecular Docking with BSA

Molecular docking study of the metal compound helps to predict their orientation and binding sites inside serum albumins. Binding interactions of the complexes with BSA are shown in Figs. 6.16-6.19. Since BSA has two different active sites (*Tyr 149* and *Tyr 410*) for binding, we performed docking of each complex with two binding sites individually in order to investigate effective binding site of BSA for our complexes.

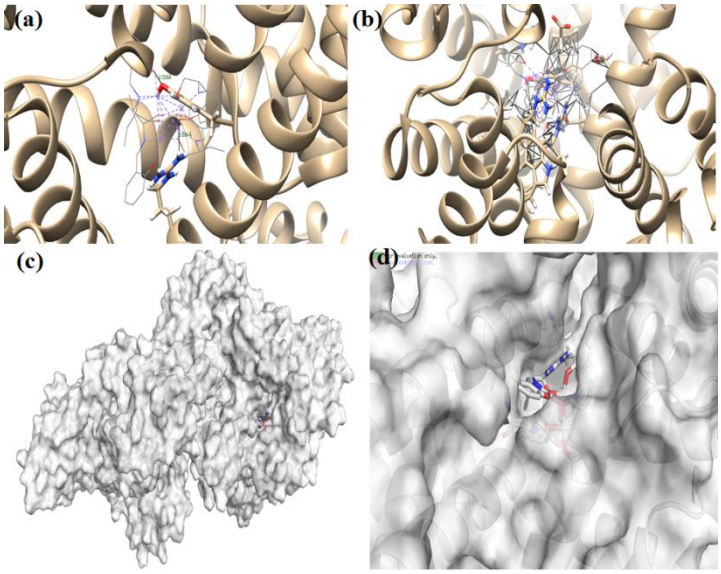

Fig. 6.16 Molecular docking image of complex **1** with BSA (binding site: Tyr149); (a) Interaction of **1** with amino acid residues of BSA (b) H-bonding interaction of **1** with amino acid residues of BSA (c) Surface plot (d) Zoom view of surface plot.

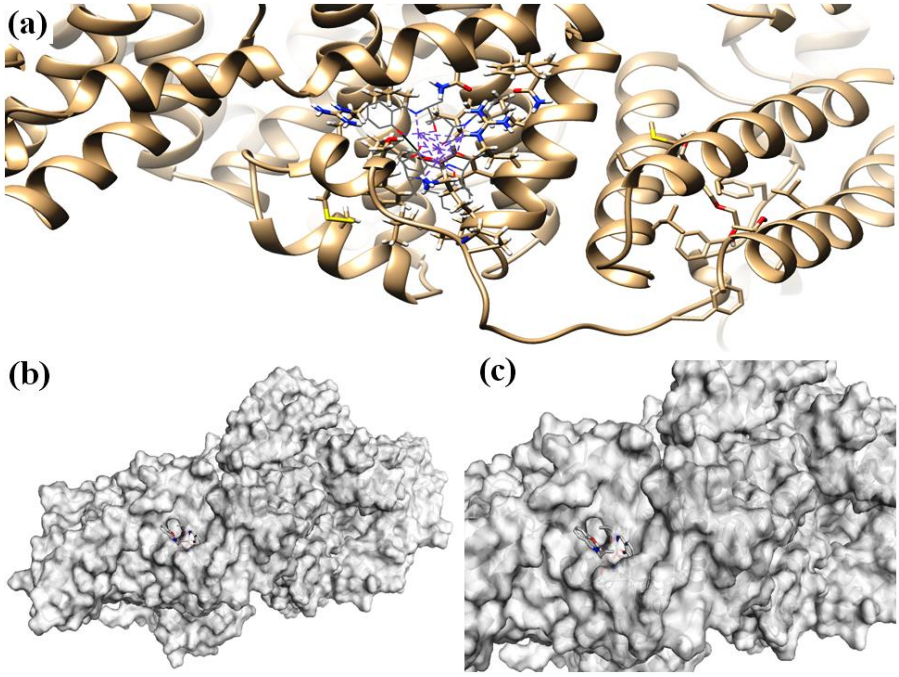

Fig. 6.17 Molecular docking image of complex **1** with BSA (binding site: Tyr410); (a) Interaction of **1** with amino acid residues of BSA (b) Surface plot (c) Zoom view of surface plot.

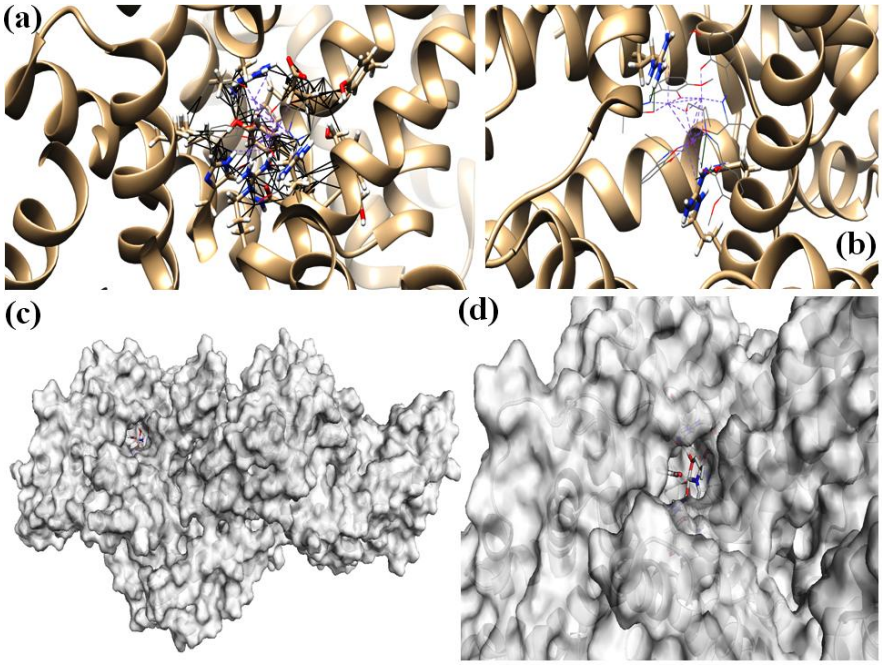

Fig. 6.18 Molecular docking image of complex **2** with BSA (binding site: Tyr149); (a) Interaction of **2** with amino acid residues of BSA (b) H-bonding interaction of **2** with amino acid residues of BSA (c) Surface plot (d) Zoom view of surface plot.

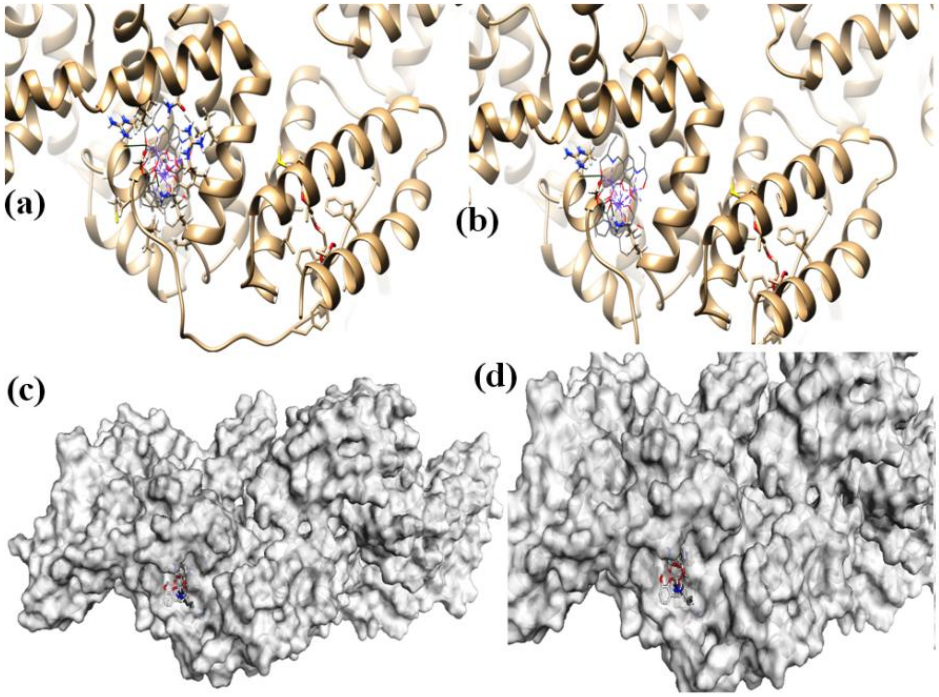

Fig. 6.19 Molecular docking image of complex **2** with BSA (binding site: Tyr410); (a) Interaction of **2** with amino acid residues of BSA (b) H-bonding interaction of **2** with amino acid residues of BSA (c) Surface plot (d) Zoom view of surface plot.

Based on chimera score (Table 6.8), it is clear that all the complexes selectively bind with BSA at the site of *Tyr 149*.

Table 6.8 Docking Chimera fitness docking scores of the copper(II) complexes with BSA.

Pose	**Chimera score**			
	*Complex **1***		*Complex **2***	
	Tyr 149	*Tyr 410*	*Tyr 149*	*Tyr 410*
1	293.8	242.2	349.8	222.4
2		242.6		

At the binding site complex **1** was surrounded by some hydrophobic amino acid residues (Ala150, Leu237, Val240, Leu210) involved in hydrophobic interactions, some polar amino acid residues (His241, Tyr149, Gln195, Trp213, Ser191, Cys244) and also present some charged amino acid residues (Arg198, Glu152, Arg256, Arg217) interact by ionic interactions (Table 6.9). One hydrogen bonding interaction was observed between the complex **1** and Arg198 [N-H (of Arg198) ⋯O (of **1**) = 2.681Å] (Table 6.10).

For interaction with **2**, there are hydrophobic contacts between **2** and some hydrophobic amino acid residues of BSA (Val240, Pro151, Ala150, Ala290, Phe148, Leu237), some polar amino acid residues (Gln195, Tyr149, His241, Ser191, Tyr156, Ser192) and some charged amino acid (Arg194, Arg198, Glu152, Arg256) (Table 6.9). Three types of hydrogen bonding interactions were observed between the complex **2** and polar amino acid residues Arg198 and Arg256 [N-H (Arg198)⋯N = 2.487Å, N-H (Arg256)⋯N = 1.607Å and N-H (Arg256)⋯O = 2.052Å] (Table 6.10).

Table 6.9 Amino acid residues in BSA which are interact with complexes.

	Charged amino acids residue	Polar amino acids residue	Hydrophobic amino acids residue
1 (Active site: Tyr149)	Arg198, Glu152, Arg256, Arg217	His241, Tyr149, Gln195, Trp213, Ser191, Cys244,	Ala150, Leu237, Val240, Leu210
1 (Active site: Tyr410)	Lys413, Arg484, Arg409	Tyr410, Ser488, Cys486, Cys475, Gln393	Phe487, Leu429, Leu406, Leu452, Leu490, Val414, Phe402, Pro492, Leu456, Asn390
2 (Active site: Tyr149)	Glu152, Arg194, Arg198, Arg256	Gln195, Tyr149, His241, Ser191, Tyr156, Ser192	Val240, Pro151, Ala150, Ala290, Phe148, Leu237
2 (Active site: Tyr410)	Lys413, Arg409, Arg484	Ser488, Tyr410, Cys486	Ala489, Phe487, Leu406, Leu386, Leu490, Asn390, Leu456, Val414

Table 6.10 Hydrogen bond interactions for complexes **1-2** with BSA.

Complex	Bonds formed	D···A (Å)	D-H···A (Å)
1 (Active site: Tyr149)	N-H (Arg198)···O	3.495	2.681
1 (Active site: Tyr410)	N-H (Leu490)···O	3.010	2.217
2 (Active site: Tyr149)	N-H (Arg198)···N	3.167	2.487
	N-H (Arg256)···N	2.375	1.607
	N-H (Arg256)···O	2.853	2.052
2 (Active site: Tyr410)	N-H (Lys413)···O	3.030	2.055

Both the serum albumins BSA and HSA consist of three major domains according to their crystal structures. These are domain I (1-195), domain II (196-383) and domain III (384-585). From the results obtained from molecular docking between BSA and complexes show that both the complexes were located in the sub domains I and II. The binding affinity order of complexes with BSA is **2** 〉 **1**. This result corroborated with the experimentally determined binding constants. The stronger binding affinity of **2** may be due to its cationic nature and more abundant hydrogen bonds between complex and polar amino acid residues (Arg198 / Arg256) of BSA.

Molecular Docking with HSA

In order to investigate effective binding site of HSA, we were performed docking of each complex with two different active sites (*Tyr 150* and *Tyr 407)* individually. Based on chimera score (Table 6.11), it is clear that both complexes **1** and **2** selectively bind with HSA at the site of

Tyr 407. Binding interactions of the complexes with the RCSB protein are shown in Figs. 6.20-6.23.

Table 6.11 Docking Chimera fitness docking scores of the copper(II) complexes with HSA.

Pose	**Chimera score**			
	*Complex **1***		*Complex **2***	
	Tyr 150	*Tyr 407*	*Tyr 150*	*Tyr 407*
1	146.1	151.9	158.9	229.4
2				230.0
3				230.7
4				231.0

Amino acids which are present nearby of the docked complexes are shown in Table 6.12 and the hydrogen bonding parameters are shown in Table 6.13. At the binding site complex **1** was surrounded by some hydrophobic amino acid residues (Leu194, Val451, Asn454, Ala190, Val340, Leu477) involved in hydrophobic interactions, some polar amino acid residues (Ser450, Trp210, Ser198, Gln455, Tyr448) and also with some charged amino acid residues (Lys191, Asp447) interact by ionic interactions (Table 6.12).

Table 6.12 Amino acid residues in BSA which are interact with complexes.

	Charged amino acids residue	Polar amino acids residue	Hydrophobic amino acids residue
1 (Active site: Tyr150)	Lys773, Arg796, Lys769, Glu727, Arg831	His241, Ser766, Tyr724, Ser861, His862, Trp788, Gln770, Ser767, His816	Phe785, Ala865, Ala768
1 (Active site: Tyr407)	Lys191, Asp447	Ser450, Trp210, Ser198, Gln455, Tyr448	Leu194, Val451, Asn454, Ala190, Val340, Leu477
2 (Active site: Tyr150)	Arg831, Lys773, Glu866, Glu727, Lys769, Arg796	His862, His816, Gln770, Ser861, Trp788, Tyr724, Ser766	Ala865, Leu812
2 (Active site: Tyr407)	Asp447, Lys191, Arg480, Glu446, Arg481, Lys195, Arg344, Arg193	Ser450, Tyr448, Trp210, Ser198	Leu194, Leu449, Val340, Leu477, Asn454, Val451, Ala197, Leu453, Val478, Phe202, Val452, Ala190, Val478

Table 6.13 Hydrogen bond interactions for complexes**1-2** with HSA.

Complex	Bonds formed	D···A (Å)	D-H···A (Å)
1 (Active site: Tyr150)	N-H (Lys769)···O	2.096	1.181
2 (Active site: Tyr150)	N-H (Lys769)···O	2.313	1.330
	N-H (Gln770)···O	3.251	2.515
2 (Active site: Tyr407)	N-H (Ser450)···O	3.043	2.186
	N-H (Leu453)···O	3.335	2.541

For interaction with **2**, there are hydrophobic contacts between **2** and some hydrophobic amino acid residues of HSA (Leu194, Leu449, Val340, Leu477, Asn454, Val451, Ala197, Leu453, Val478, Phe202, Val452, Ala190, Val478), some polar amino acid residues (Ser450, Tyr448, Trp210, Ser198) and charged amino acid residues (Asp447, Lys191, Arg480, Glu446, Arg481, Lys195, Arg344, Arg193) (Table 6.12). Two hydrogen bonding interactions were observed between the complex **2** and amino acid residues Ser450 and Leu453 [N-H (Ser450)···O = 2.186Å and N-H (Leu453)···O = 2.541Å] (Table 6.13).

From these results it can be inferred that the complexes **1** and **2** were located in the sub domains II and III of HSA. The molecular docking results also indicate that the binding affinity of complexes is in the order **2** 〉 **1** which corroborate the experimental results. Different binding affinities may be due to the presence of different numbers of hydrophobic amino acids residues interacting in the binding cavity of the complexes. A total thirteen hydrophobic amino acids were present in the cavity site of **2** and involved in the binding process, whereas the number of hydrophobic amino acids are six for **1**.

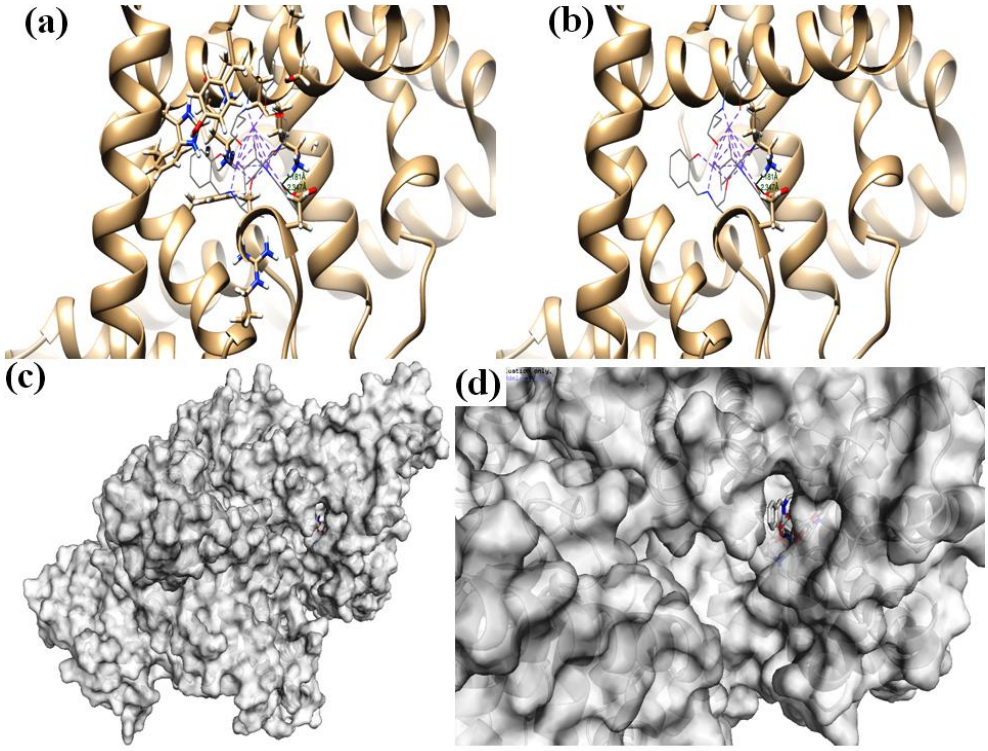

Fig. 6.20 Molecular docking image of complex **1** with HSA (binding site: Tyr150); (a) Interaction of **1** with amino acid residues of HSA (b) H-bonding interaction of **1** with amino acid residues of HSA (c) Surface plot (d) Zoom view of surface plot.

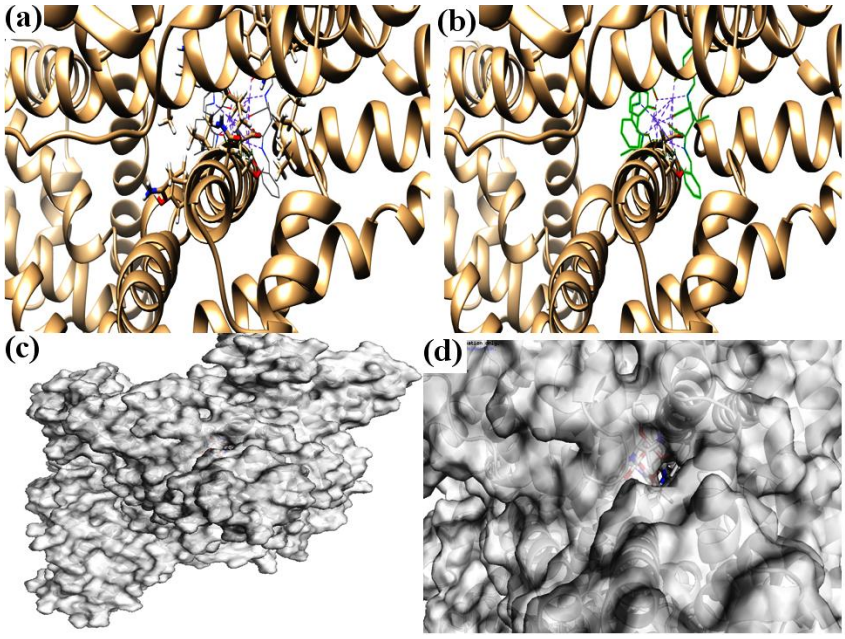

Fig. 6.21 Molecular docking image of complex **1** with HSA (binding site: Tyr407); (a) Interaction of **1** with amino acid residues of HSA (b) H-bonding interaction of **1** with amino acid residues of HSA (c) Surface plot (d) Zoom view of surface plot.

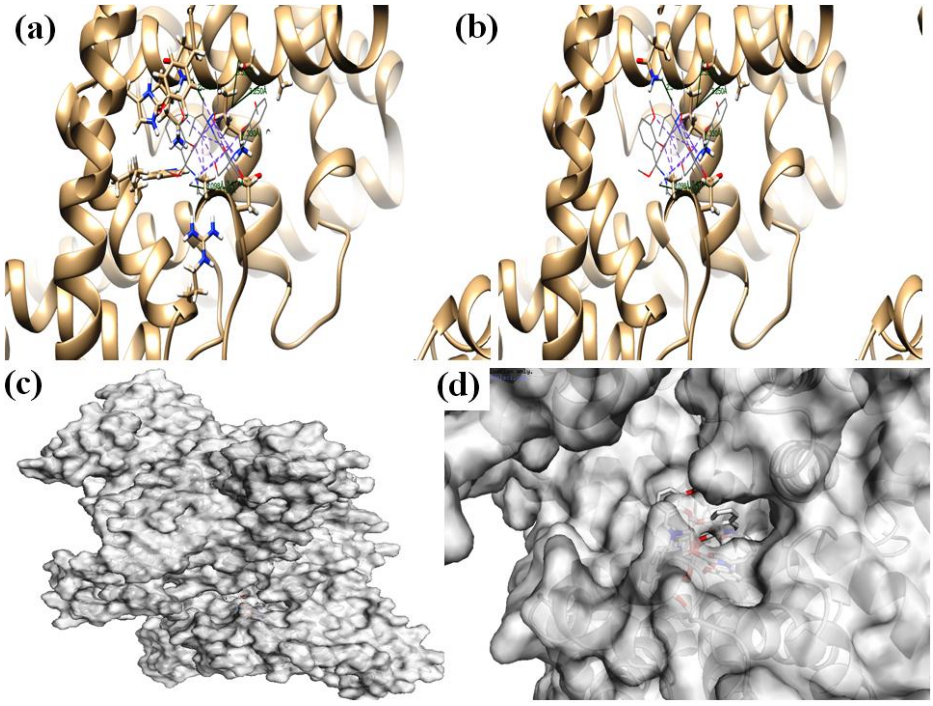

Fig. 6.22 Molecular docking image of complex **2** with HSA (binding site: Tyr150); (a) Interaction of **2** with amino acid residues of HSA (b) H-bonding interaction of **2** with amino acid residues of HSA (c) Surface plot (d) Zoom view of surface plot.

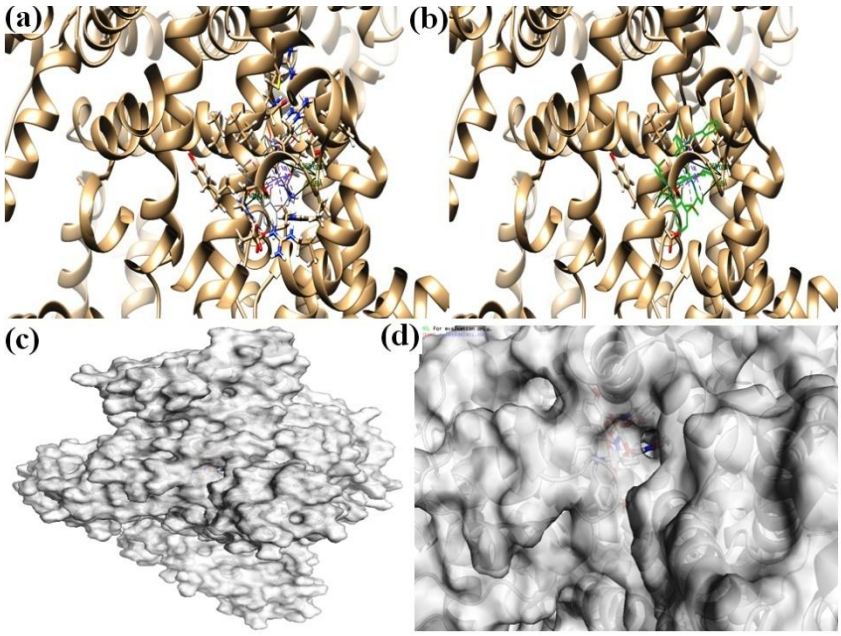

Fig. 6.23 Molecular docking image of complex **2** with HSA (binding site: Tyr407); (a) Interaction of **2** with amino acid residues of HSA (b) H-bonding interaction of **2** with amino acid residues of HSA (c) Surface plot (d) Zoom view of surface plot.

6.4 Conclusion

In summary, we have presented here synthesis, crystal structure, low temperature magnetic behaviour and serum albumin / CT-DNA interactions of tetranuclear close cubane core (**1**) and tetranuclear double-open cubane core (**2**) copper(II) complexes. Variable temperature (2 - 300 K) magnetic susceptibility measurements of both the complexes indicate antiferromagnetic exchange coupling between copper centres, which is in full agreement with their structure. Studies of the interaction of complexes with serum albumins indicate that the complexes interact with serum albumins through ground state association process. UV-vis absorption and fluorescence spectroscopic study indicate that the interaction of complexes with CT-DNA occur with intercalation/groove binding mode. Molecular docking study confirm that the interaction of complexes with CT-DNA occur through groove binding.